

## MID-INFRARED EXTINCTION MAPPING OF INFRARED DARK CLOUDS: PROBING THE INITIAL CONDITIONS FOR MASSIVE STARS AND STAR CLUSTERS

MICHAEL J. BUTLER AND JONATHAN C. TAN

Department of Astronomy, University of Florida, Gainesville, FL 32611, USA;  
butler85@astro.ufl.edu, jt@astro.ufl.edu

*Draft version September 11, 2021*

### ABSTRACT

Infrared Dark Clouds (IRDCs) are cold, dense regions of giant molecular clouds that are opaque at wavelengths  $\sim 10\ \mu\text{m}$  or more and thus appear dark against the diffuse Galactic background emission. They are thought to be the progenitors of massive stars and star clusters. We use  $8\ \mu\text{m}$  imaging data from *Spitzer* GLIMPSE to make extinction maps of 10 IRDCs, selected to be relatively nearby and massive. The extinction mapping technique requires construction of a model of the Galactic IR background intensity behind the cloud, which is achieved by correcting for foreground emission and then interpolating from the surrounding regions. The correction for foreground emission can be quite large, up to  $\sim 50\%$  for clouds at  $\sim 5\ \text{kpc}$  distance, thus restricting the utility of this technique to relatively nearby clouds. We investigate three methods for the interpolation, finding systematic differences at about the 10% level, which, for fiducial dust models, corresponds to a mass surface density  $\Sigma = 0.013\ \text{g cm}^{-2}$ , above which we conclude this extinction mapping technique attains validity. We examine the probability distribution function of  $\Sigma$  in IRDCs. From a qualitative comparison with numerical simulations of astrophysical turbulence, many clouds appear to have relatively narrow distributions suggesting relatively low ( $< 5$ ) Mach numbers and/or dynamically strong magnetic fields. Given cloud kinematic distances, we derive cloud masses. Rathborne, Jackson & Simon identified cores within the clouds and measured their masses via mm dust emission. For 43 cores, we compare these mass estimates with those derived from our extinction mapping, finding good agreement: typically factors of  $\lesssim 2$  difference for individual cores and an average systematic offset of  $\lesssim 10\%$  for the adopted fiducial assumptions of each method. We find tentative evidence for a systematic variation of these mass ratios as a function of core density, which is consistent with models of ice mantle formation on dust grains and subsequent grain growth by coagulation, and/or with a temperature decrease in the densest cores.

*Subject headings:* ISM: clouds, dust, extinction — stars: formation

### 1. INTRODUCTION

Large fractions of stars form in clusters from the densest *clumps* within giant molecular clouds (GMCs) (Lada & Lada 2003). These regions are also responsible for the birth of essentially all massive stars (de Wit et al. 2005). It is possible that our own solar system formed in such a region near a massive star (Hester et al. 2004), so the process of massive star and star cluster formation may be directly involved in our own origins. Understanding the formation of star clusters is also important as a foundation for understanding global galactic star formation rates (Kennicutt 1998) and thus the evolution of galaxies.

In spite of this importance, there are many gaps in our knowledge of how massive stars and star clusters are formed. For massive star formation there is a basic debate about whether the process is simply a scaled-up version of low-mass star formation from gas cores (Shu, Adams, Lizano 1987), albeit requiring the high pressures found in the centers of star-forming clumps (McKee & Tan 2003), or whether a qualitatively different mechanism is involved, such as stellar collisions (Bonnell, Bate, Zinnecker 1998) or competitive Bondi-Hoyle accretion (Bonnell et al. 2001; Bonnell, Vine, & Bate 2004). A prediction of the scenario involving formation from cores is the presence of massive, gravitationally-bound starless cores as initial conditions.

For star cluster formation there is a debate about

whether the *protocluster* (or *star-forming clump*) is in quasi-virial equilibrium (Tan, Krumholz, & McKee 2006) or is undergoing rapid global collapse (Elmegreen 2000, 2007; Hartmann & Burkert 2007). This corresponds to a debate about the timescale of star cluster formation: does it take many or just a few free-fall times?

To help resolve these issues we require knowledge about the initial conditions of massive star and star cluster formation. The star-forming clumps that are the sites of these processes have typically been identified from the radiative emission and activity of their young stars: e.g. radio emission from ultracompact H II regions created by massive stars or maser emission from hot, dense gas near massive protostars. Unfortunately by the time this activity signposts the region, it has typically also erased much of the memory of the initial conditions from the system. This is especially true of protostellar outflows, which have a mechanical power large enough to significantly stir the gas of the star-forming clump and halt any large scale gravitational collapse (Nakamura & Li 2007).

The initial conditions for massive star and star cluster formation are expected to be dense, cold cores and clumps of gas. In some formation models there may be of order hundreds of solar masses of gas compressed to within a few tenths of a parsec. For a spherical cloud the

mean mass surface density,  $\Sigma$ , in this case is

$$\Sigma \equiv \frac{M_c}{\pi R_c^2} = 0.665 \frac{M_c}{100 M_\odot} \left( \frac{R_c}{0.1 \text{ pc}} \right)^{-2} \text{ g cm}^{-2}. \quad (1)$$

For reference,  $\Sigma = 1 \text{ g cm}^{-2}$  corresponds to  $4800 M_\odot \text{ pc}^{-2}$ ,  $N_{\text{H}} = 4.3 \times 10^{23} \text{ cm}^{-2}$  and  $A_V \simeq 230 \text{ mag}$ , for local diffuse ISM dust properties (e.g. Draine 2003). The extension of the extinction law into the mid-infrared (MIR) is somewhat controversial and uncertain (Lutz et al. 1996; Draine 2003; Indebetouw et al. 2005; Román-Zúñiga et al. 2007), but nevertheless, such column densities are expected to correspond to several magnitudes of extinction at  $8 \mu\text{m}$ .

Such Infrared Dark Clouds (IRDCs) have been identified in images of the Galactic plane from the *Infrared Space Observatory* (ISO) (Pérault et al. 1996), the *Mid-course Space Experiment* (MSX) (Egan et al. 1998). Simon et al. (2006a) identified about 10,000 potential IRDCs from intensity contrast features in the MSX survey. Simon et al. (2006b) identified the  $^{13}\text{CO}$  emission from about 300 of the darkest of these in the Galactic Ring Survey (GRS) (Jackson et al. 2006), thus deriving their kinematic distances. Rathborne, Jackson, & Simon (2006) surveyed the 1.2 mm dust continuum emission from 38 of these IRDCs, identifying 140 mm-emission cores within these clouds.

The temperatures in IRDCs are measured to be  $\lesssim 20 \text{ K}$  (Carey et al. 1998). High deuteration fractions have been reported by Pillai et al. (2007). Under these conditions one expects high depletion of volatiles onto ice mantles of dust grains (Dalgarno & Lepp 1984). Larger molecular line surveys of IRDCs have been carried out by, for example, Ragan et al. (2006) and Sakai et al. (2008).

In this paper we present a method of extinction mapping of IRDCs using the diffuse Galactic IR emission observed by *Spitzer* as the background source. This method complements that based on measuring the extinction to individual stars (e.g. Román-Zúñiga et al. 2007), by providing a measurement of the extinction at the location of almost every pixel in the cloud image, including at very high column densities, thus allowing a detailed investigation of the cloud structure.

## 2. IRDC SAMPLE SELECTION

Considering *Spitzer* Galactic Legacy Mid-Plane Survey Extraordinaire (GLIMPSE) (Benjamin et al. 2003)  $8 \mu\text{m}$  (i.e. Infrared Array Camera [IRAC] band 4) images, we chose 10 IRDCs from the sample of Rathborne et al. (2006), selecting those that were relatively nearby, massive, dark (i.e. showing high contrast compared to the surrounding diffuse emission), and/or with relatively simple surrounding diffuse emission. The properties of these clouds are listed in Table 1. Apart from being relatively nearby, this sub-sample is in fact fairly representative of the full 38 cloud sample of Rathborne et al. (2006).

Simon et al. (2006a) fit ellipses to each cloud based on MSX images. While these ellipses are often not particularly accurate descriptions of the IRDC shapes, we will utilize them as convenient measures of the approximate sizes and shapes of the clouds, especially for the small scale median filter method of estimating the background radiation (§3.2.2).

The *Spitzer* telescope has an angular resolution (PSF FWHM) of about  $2''$  at  $8 \mu\text{m}$ , which corresponds to a linear scale of  $0.029 \text{ pc}$  for a cloud at a distance of  $3 \text{ kpc}$ . Note, GLIMPSE images are processed to a pixel scale corresponding to an angular resolution of  $1.2''$ .

## 3. IRDC EXTINCTION MAPPING METHODS

The extinction mapping technique requires knowing the intensity of radiation directed towards the observer at a location behind the cloud of interest,  $I_{\nu,0}$ , and just in front of the cloud,  $I_{\nu,1}$ . Then for negligible emission in the cloud and a simplified 1D geometry,

$$I_{\nu,1} = I_{\nu,0} \exp(-\tau_\nu), \quad (2)$$

where the optical depth  $\tau_\nu = \kappa_\nu \Sigma$ , where  $\kappa_\nu$  is the total opacity at frequency  $\nu$  per unit gas mass and  $\Sigma$  is the gas mass surface density.

To evaluate  $\kappa_\nu$  appropriate for the various intensities measured by the *Spitzer Space Telescope*, namely the 4 IRAC bands and the Multiband Imaging Photometer (MIPS)  $24 \mu\text{m}$  band, we adopt a spectrum of the diffuse Galactic IR emission from Li & Draine (2001), the filter response functions of the IRAC and MIPS bands, and perform an intensity and filter response weighted average of the opacity of various dust models (Figure 1 & Table 2). Uncertainties in the dust models include the extent to which ice mantles have formed on the grains and the extent to which the grains have undergone coagulation.

The IR background in the wavelength range probed by the IRAC bands receives its greatest contribution from the diffuse ISM (transiently heated small grains) at Band 4, i.e.  $\sim 8 \mu\text{m}$ , compared to that from background stars. Individual stellar sources become much more prominent in the GLIMPSE images at the shorter wavelengths. Thus in this paper we restrict our analysis to Band 4 images, leaving analysis at other wavelengths and the wavelength dependence of extinction for a future study.

In the  $8 \mu\text{m}$  band, we estimate a range of dust opacities per gas mass of  $6.3 - 11 \text{ cm}^2 \text{ g}^{-1}$ , and adopt  $\kappa_\nu = 7.5 \text{ cm}^2 \text{ g}^{-1}$ , which is formally closest to the model of Ossenkopf & Henning (1994) with thin ice mantles that have undergone coagulation for  $10^5 \text{ yr}$  at a density of  $n_{\text{H}} = 10^6 \text{ cm}^{-3}$  (or approximately equivalent to  $10^6 \text{ yr}$  at  $n_{\text{H}} = 10^5 \text{ cm}^{-3}$ , etc.).

We estimate  $I_{\nu,0}$  via interpolation from the regions surrounding the particular IRDC of interest. These interpolation methods, which necessarily involve an averaging over small scale spatial variations in  $I_{\nu,0}$ , are described below in §3.2. We evaluate  $I_{\nu,1}$  from the observed intensities derived from the cloud images. First we consider the effects of foreground dust emission.

### 3.1. Correction for Foreground Dust Emission

Our determinations of both  $I_{\nu,0}$  and  $I_{\nu,1}$  are potentially affected by foreground emission from hot dust. We estimate the size of this effect given the (kinematic) distance to the cloud and a model for the Galactic distribution of hot dust emission, assuming it is the same as the distribution of the Galactic surface density of OB associations (McKee & Williams 1997):

$$\Sigma_{\text{OB}} \propto \exp\left(-\frac{R}{H_{\text{R}}}\right), \quad (3)$$

TABLE 1  
INFRARED DARK CLOUD SAMPLE<sup>a</sup>

Cloud Name	$l$ ( $^{\circ}$ )	$b$ ( $^{\circ}$ )	Distance (kpc)	$R_{\text{eff}}$ (pc)	$e$	P.A. ( $^{\circ}$ )	$f_{\text{fore}}$	$\Sigma_{\text{SMF}}^{\text{b}}$ ( $\text{g cm}^{-2}$ )	$M_{\text{LMF}}$ ( $M_{\odot}$ )	$M_{\text{SMF}}$ ( $M_{\odot}$ )
A (G018.82−00.28)	18.822	−0.285	4.8	10.4	0.961	74	0.209	0.0355	6,700	7,600
B (G019.27+00.07)	19.271	0.074	2.4	2.71	0.977	88	0.075	0.0387	930	830
C (G028.37+00.07)	28.373	0.076	5.0	15.4	0.632	78	0.266	0.0527	27,000	42,000
D (G028.53−00.25)	28.531	−0.251	5.7	16.9	0.968	60	0.327	0.0418	17,400	27,000
E (G028.67+00.13)	28.677	0.132	5.1	11.5	0.960	103	0.276	0.0543	15,100	19,400
F (G034.43+00.24)	34.437	0.245	3.7	3.50	0.926	79	0.193	0.0371	1,770	1,670
G (G034.77−00.55)	34.771	−0.557	2.9	3.06	0.953	95	0.140	0.0420	1,050	1,140
H (G035.39−00.33)	35.395	−0.336	2.9	9.69	0.951	59	0.142	0.0262	4,000	6,800
I (G038.95−00.47)	38.952	−0.475	2.7	3.73	0.917	64	0.141	0.0616	880	1,490
J (G053.11+00.05)	53.116	0.054	1.8	0.755	0.583	50	0.121	0.0699	108	80

<sup>a</sup>Coordinate names, Galactic coordinates, kinematic distances, effective radii (of equal area circles), eccentricities and position angles of fitted ellipses are from Simon et al. (2006a).

<sup>b</sup>This estimate of mean mass surface density, used to normalize the distributions in Fig. 11, is the areal average of those pixels for which values of  $\Sigma_{\text{SMF}} > 0$  are derived. Estimates of a mean mass surface density based on  $M_{\text{SMF}}$  and  $R_{\text{eff}}$  are typically much smaller because of the regions inside the clouds ellipses with  $\Sigma_{\text{SMF}} \leq 0$ .

TABLE 2  
SPITZER TELESCOPE BAND AND BACKGROUND-WEIGHTED DUST OPACITIES PER GAS MASS ( $\text{cm}^2 \text{g}^{-1}$ )

Dust Model <sup>a</sup>	IRAC Band 1 $3.5\mu\text{m}^{\text{b}}$	IRAC Band 2 $4.5\mu\text{m}$	IRAC Band 3 $5.9\mu\text{m}$	IRAC Band 4 $7.8\mu\text{m}$	MIPS Band 1 $23.0\mu\text{m}$
WD01 $R_V = 3.1$	10.02	6.26	4.16	6.25	4.50
WD01 $R_V = 3.1$ flat IR bkg <sup>c</sup>	9.78	6.20	4.25	7.71	4.24
WD01 $R_V = 5.5$	15.56	10.24	6.55	8.27	5.54
WD01 $R_V = 5.5$ case B	14.23	11.49	9.25	10.96	6.01
OH94 thin mantle, 0 yr	17.52 (12.69)	10.68 (8.69)	7.78 (7.06)	6.26 (6.15)	4.43
OH94 thin mantle, $10^5 \text{yr}$ , $10^6 \text{cm}^{-3}$	22.41 (16.23)	13.31 (10.83)	9.44 (8.56)	7.48 (7.34)	6.23

<sup>a</sup>References: WD01 - Weingartner & Draine (2001); OH94 - Ossenkopf & Henning (1994), opacities have been scaled from values in parentheses to include contribution from scattering.

<sup>b</sup>Mean wavelengths weighted by filter response and background spectrum.

<sup>c</sup>No weighting made for spectrum of Galactic diffuse emission.

where  $R$  is the galactocentric radius and  $H_R = 3.5$  kpc is the radial scale length. For each IRDC, given its distance and Galactic longitude, we calculate the ratio of the column of hot dust between the solar position (at  $R = 8$  kpc) and the total column extending out to a galactocentric radius of 16 kpc. This “Foreground Intensity Ratio”,  $f_{\text{fore}}$ , is listed in Table 1 for each IRDC. Then we derive an estimate of the true intensity of the radiation field just behind the cloud,  $I_{\nu,0}$ , from that measured via interpolation of the cloud images,  $I_{\nu,0,\text{obs}}$ , via

$$I_{\nu,0} = (1 - f_{\text{fore}})I_{\nu,0,\text{obs}}. \quad (4)$$

We also estimate the true intensity of the radiation field just in front of the cloud,  $I_{\nu,1}$  from that measured directly from the cloud images,  $I_{\nu,1,\text{obs}}$ , via

$$I_{\nu,1} = I_{\nu,1,\text{obs}} - f_{\text{fore}}I_{\nu,0,\text{obs}}. \quad (5)$$

Typical values of  $f_{\text{fore}}$  are about 15%, with values up to 33% for the most distant cloud, D, at 5.7 kpc. As an example of the size of the corrections to  $\Sigma$  resulting from the foreground subtraction, consider cloud C, for which  $f_{\text{fore}} = 0.266$ ,  $I_{\nu,0,\text{obs}} \simeq 100 \text{ MJy sr}^{-1}$  and  $I_{\nu,1,\text{obs}} \simeq 50 \text{ MJy sr}^{-1}$  in the darkest part of the cloud. For these regions, one would derive  $\Sigma \simeq 0.092 \text{ g cm}^{-2}$  without the foreground correction and  $\Sigma \simeq 0.152 \text{ g cm}^{-2}$  with this correction.

Our estimate of  $f_{\text{fore}}$  is uncertain due to small scale spatial variations in the hot dust emission in the Galaxy. Also, we are typically measuring  $I_{\nu,0,\text{obs}}$  from regions relatively close to the IRDC of interest. Such regions are likely to overlap with the GMC hosting the IRDC, and thus have higher than average extinction of the integrated Galactic background emission. This will cause us to tend to underestimate  $f_{\text{fore}}$  and thus  $\Sigma$ . An upper limit to  $f_{\text{fore}}$  is provided by the minimum value of  $I_{\nu,1,\text{obs}}$  for each cloud. For example, for Cloud C this is about  $40 \text{ MJy sr}^{-1}$  intensity units, so that for a background of  $100 \text{ MJy sr}^{-1}$ , the maximum value of  $f_{\text{fore}} \simeq 0.4$ . Uncertainties in  $f_{\text{fore}}$  are one of the major reasons for restricting the extinction mapping analysis to relatively nearby clouds.

### 3.2. Background Estimation

#### 3.2.1. Large-Scale Median Filter (LMF)

A relatively simple way of estimating the diffuse IR background at a given location behind an IRDC is to take a median average of a region (i.e. filter) centered on the location of interest and that is large compared to the cloud. This method was applied by Simon et al. (2006a) to model the Galactic background from *MSX* images to then identify IRDCs as high contrast features.

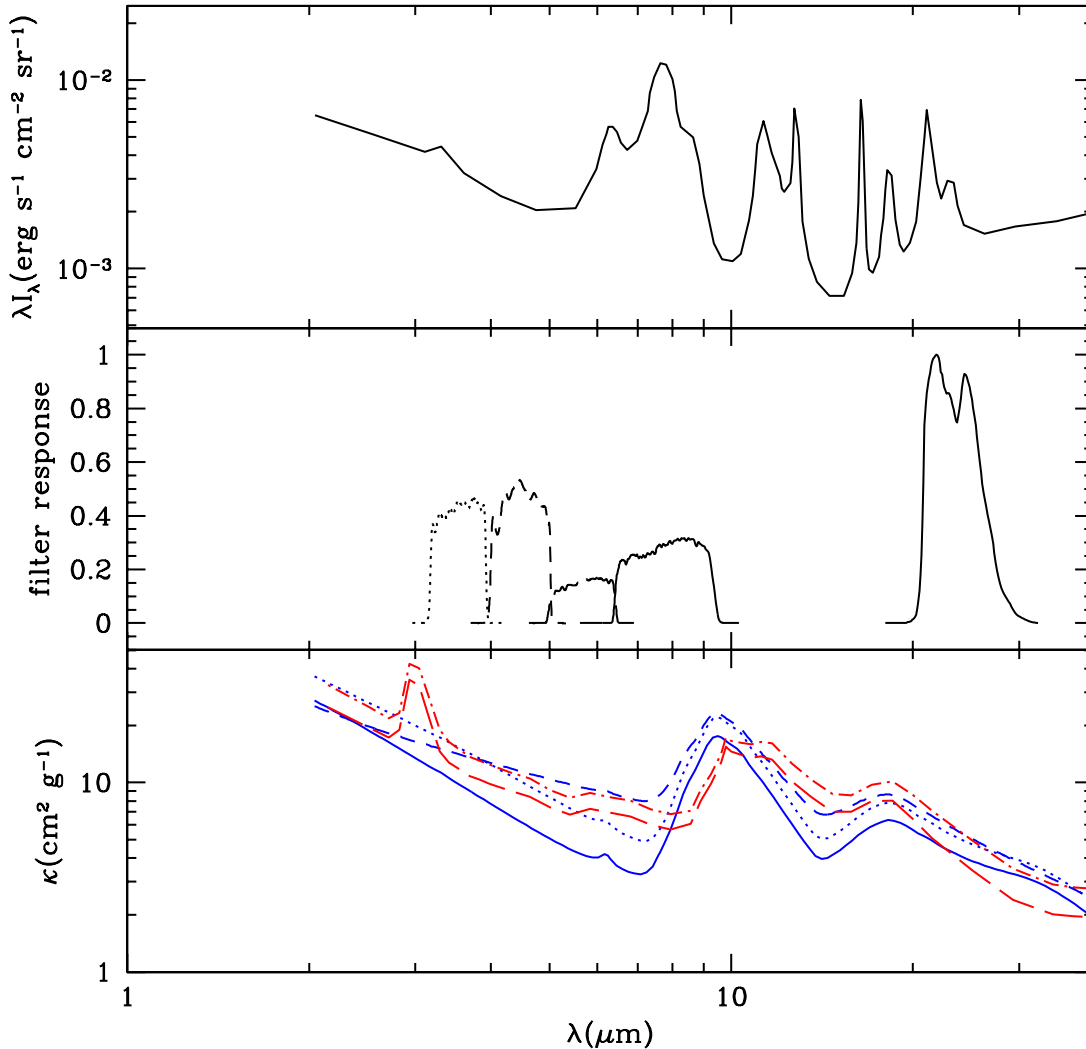


FIG. 1.— *Top*: Adopted spectrum of diffuse IR background from the “MIRS” region in the Galactic plane at  $l \simeq 44^\circ$  modeled by Li & Draine (2001). *Middle*: Filter response of IRAC bands 1-4 and the MIPS 24  $\mu\text{m}$  band. *Bottom*: Dust opacities (per gas mass) from Weingartner & Draine (2001) as updated by Draine (2003): Model with  $R_V = 3.1$  (solid line),  $R_V = 5.5$  (dotted line),  $R_V = 5.5$  case B (dashed line). These opacities include scattering, which is about a 40% of total effect at 3  $\mu\text{m}$ , but only a 2% effect at 8  $\mu\text{m}$ . The long-dashed line shows the thin ice mantle MRN model (only contribution from  $\kappa_{\text{abs}}$  per gas mass is shown) of Ossenkopf & Henning (1994). The dot-dashed line shows this model after  $10^5$  yr of coagulation at a density of  $n_{\text{H}} = 10^6 \text{ cm}^{-3}$ . The background and filter-weighted opacities are listed in Table 2.

This method will only capture background fluctuations on scales larger than the cloud. Indeed if the filter becomes too small, i.e. with a size comparable to the cloud, then the derived background will become influenced by the cloud itself and will be underestimated.

For simplicity, we adopt a square-shaped filter for this method. After some experimentation and given the sizes of the IRDCs in our sample, we chose a filter size of  $13'$ , i.e. 650 Spitzer-GLIMPSE image pixels. We evaluate the background on a uniform grid with spacings of  $24''$ . At each location, we first consider the full distribution of pixel intensities, and evaluate the mode. Since the high-end tail of this distribution, due to extended bright sources and stars, was typically much larger than the

low-end tail, due to the IRDC, we excluded pixels that had intensities twice the value of the mode, and then found the median value of the remaining distribution. This value was assigned to  $I_{\nu,0,\text{obs}}$  for all the pixels in the  $24'' \times 24''$  square sharing the same center as the  $13'$  filter. This Large Scale Median Filter (LMF) method is illustrated for cloud C in the left-hand panels of Figure 2. The distribution of pixel intensities is shown in Figure 3.

Note that there will be some regions where the estimated value of  $I_{\nu,1}$  is greater than that of  $I_{\nu,0}$ . This can arise because of foreground or background stars, or because of small fluctuations in the true background intensity that are not captured by the large scale averaging used in the model. Examining the distribution of intensi-

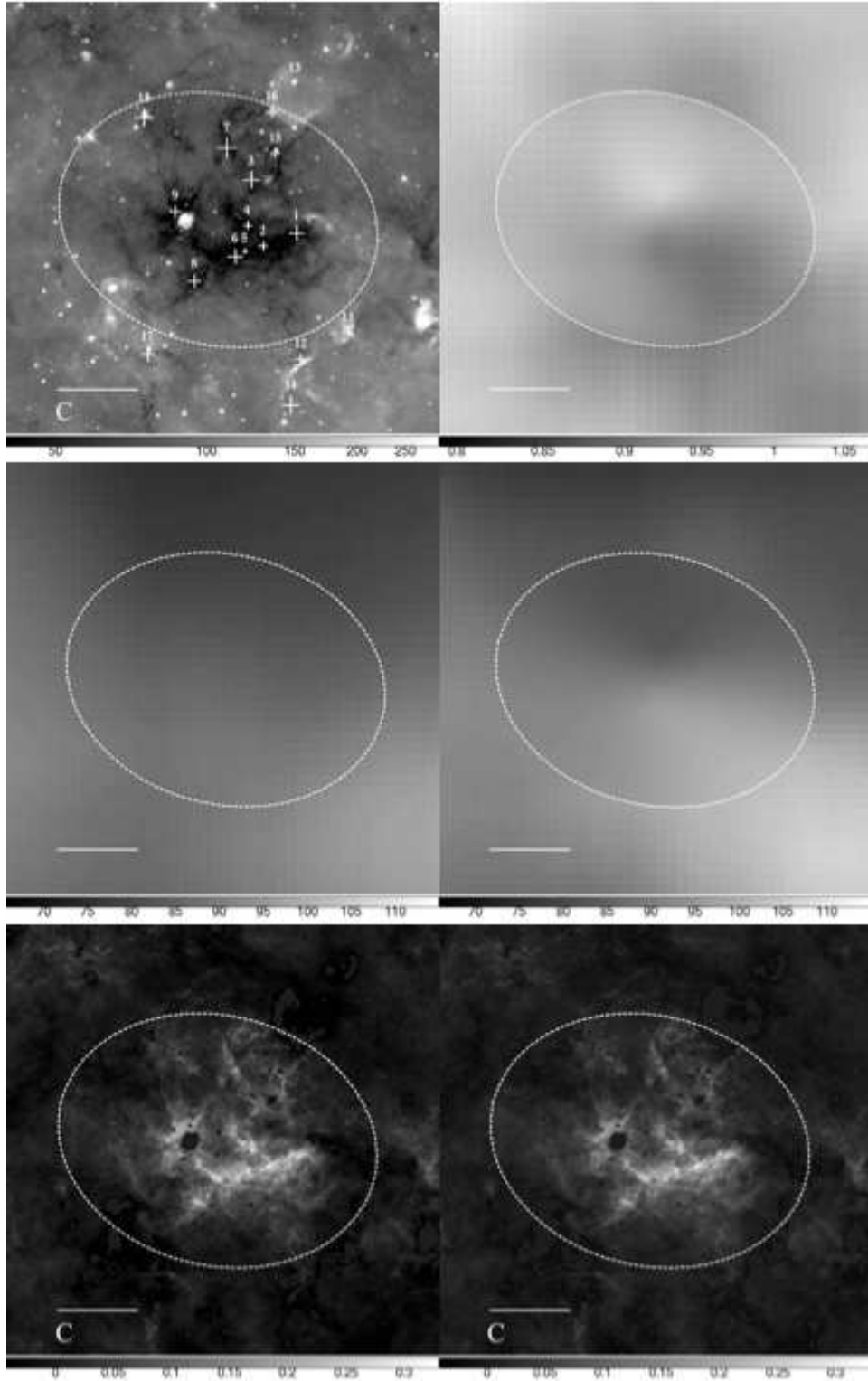


FIG. 2.— *Top left*: Spitzer IRAC  $8\mu\text{m}$  image of Cloud C (G028.37+00.07) (logarithmic intensity scale in units of  $\text{MJy sr}^{-1}$ ), with the dashed ellipse defined by Simon et al. (2006a) (based on MSX images), the crosses showing mm emission cores (Rathborne et al. 2006), and the horizontal line showing a scale of  $3'$  and the intensity scale in  $\text{MJy sr}^{-1}$ . *Middle left*: Large-scale Median Filter (LMF) estimate of  $I_{\nu,0,\text{obs}}$  (linear intensity scale in units of  $\text{MJy sr}^{-1}$ ). *Bottom left*: LMF estimate of  $\Sigma$  (intensity scale in units of  $\text{g cm}^{-2}$ ). *Top right*:  $I_{\nu,0,\text{obs,LMF}}/I_{\nu,0,\text{obs,SMF}}$ . *Middle right*: Small-scale Median Filter (SMF) estimate of  $I_{\nu,0,\text{obs}}$ . *Bottom right*: SMF estimate of  $\Sigma$ .

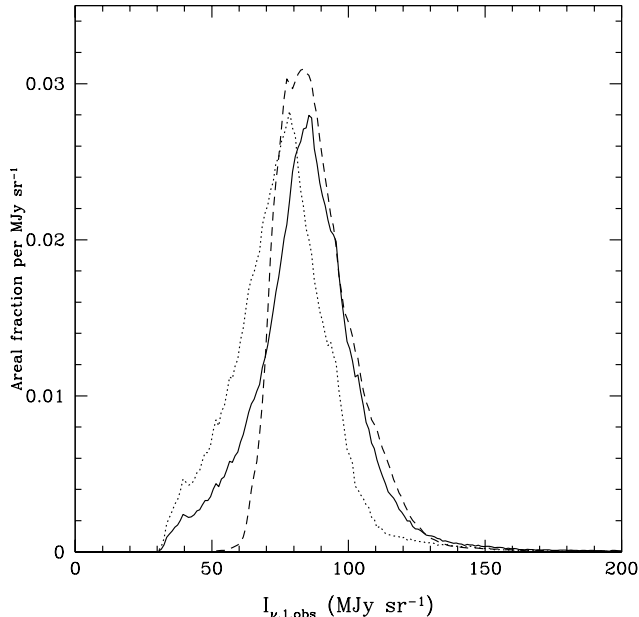


FIG. 3.— Distribution of pixel intensities for Cloud C. The solid line shows the distribution inside the LMF ( $13'$  by  $13'$ ) centered on the IRDC. The dotted line shows the distribution inside the IRDC ellipse and the dashed line shows it outside the ellipse (for a region  $24'$  square).

ties in the LMF, we find the FWHM of the distribution. We set those pixels with  $I_{\nu,1} > I_{\nu,0} + 0.5\text{FWHM}$ , equal to  $I_{\nu,0}$  so that the derived  $\Sigma$  at this location is zero. These regions are typically stars or bright emission regions. The remaining pixels with  $I_{\nu,1} > I_{\nu,0}$  are allowed to yield a negative value of  $\Sigma$ , which helps prevent small scale fluctuations (which can include instrument noise) from biasing the total mass in a region to positive values.

### 3.2.2. Small-Scale Median Filter (SMF)

In order to resolve smaller-scale variations in the IR background, but without having the median filter estimate be affected by the IRDC, we develop a second method, which uses a small-scale median filter in regions outside a defined cloud boundary and an interpolation scheme inside this boundary. For cloud boundaries, we utilize the ellipses defined by Simon et al. (2006a) from their study of MSX images of the clouds. We set the filter size to be one third of the major axis of this ellipse. The method of estimating the median pixel intensity used for the LMF (§3.2.1) is repeated for the region outside the cloud ellipse.

For each image pixel inside the IRDC ellipse we estimate  $I_{\nu,0,\text{obs}}$  by interpolating from values of  $I_{\nu,0,\text{obs}}$  outside of the ellipse that are within an angular distance equal to the semi-major axis of the ellipse, weighting by the inverse square of the angular separation, so that the innermost annuli dominate the average. This Small-Scale Median Filter (SMF) method is illustrated for cloud C in the right-hand panels of Figure 2. Here, and also in Figure 4, we compare the LMF and SMF estimates of  $I_{\nu,0}$ , finding typical variations at the level of  $\lesssim 10\%$ . A 10% uncertainty in  $I_{\nu,0}$  corresponds to a mass surface density

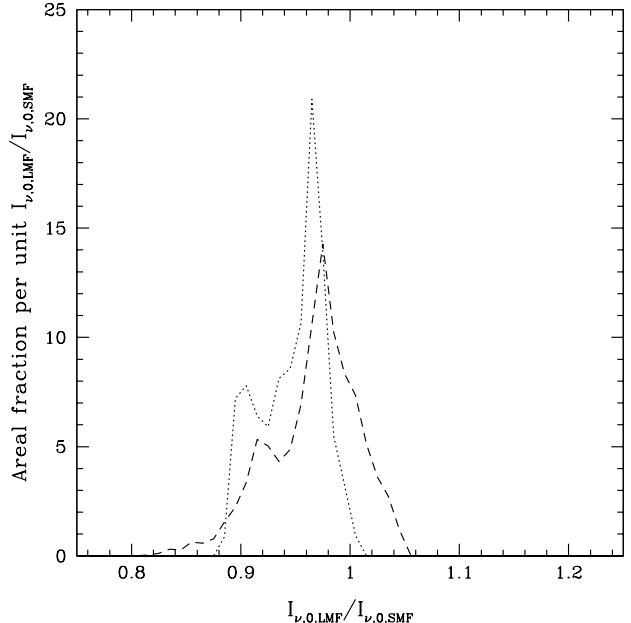


FIG. 4.— Distribution of the ratio ( $I_{\nu,0,\text{LMF}}/I_{\nu,0,\text{SMF}}$ ) of background intensities derived from of LMF and SMF methods. The dotted and dashed lines show the distribution inside and outside (for a region  $24'$  square) the cloud ellipse, respectively.

of  $0.013 \text{ g cm}^{-2}$ . We conclude that systematic uncertainties in background estimation set a minimum threshold  $\Sigma$ , below which the mid-IR extinction mapping method becomes unreliable.

Here, we also note that the GLIMPSE images are occasionally prone to certain artifacts, e.g. changes in diffuse intensity along diagonal bands and stripes (see cloud B and D images below), which will introduce additional uncertainties in these regions. The SMF method improves upon the LMF method in reducing the effect of these artifacts.

### 3.2.3. Orthogonal Strips Across Filamentary IRDCs

To further test the accuracy of the LMF and SMF methods, we consider the structure of the IR background on very small scales across a filamentary IRDC (cloud H). We choose two strips, approximately orthogonal to regions of the IRDC that are very filamentary (i.e. thin) and free of stars (see Figure 5). The median image intensities are evaluated along these strips (Figure 6). A linear fit for the IR background is fit to regions of the strip judged to be free of cloud material. This is a somewhat subjective process, since it is hard to distinguish between small-scale background variations and additional absorbing components. Nevertheless, we expect this estimate of the background intensity just behind the filament to be more accurate than the LMF and SMF methods, because the interpolation behind the filament is over a very small angular scale (about a few tens of arcseconds) and the background appears to be quite smooth in this general region.

The ratio of the LMF and SMF estimates of the background across the strips is compared to that directly estimated from the strips is shown in Figure 6. We also

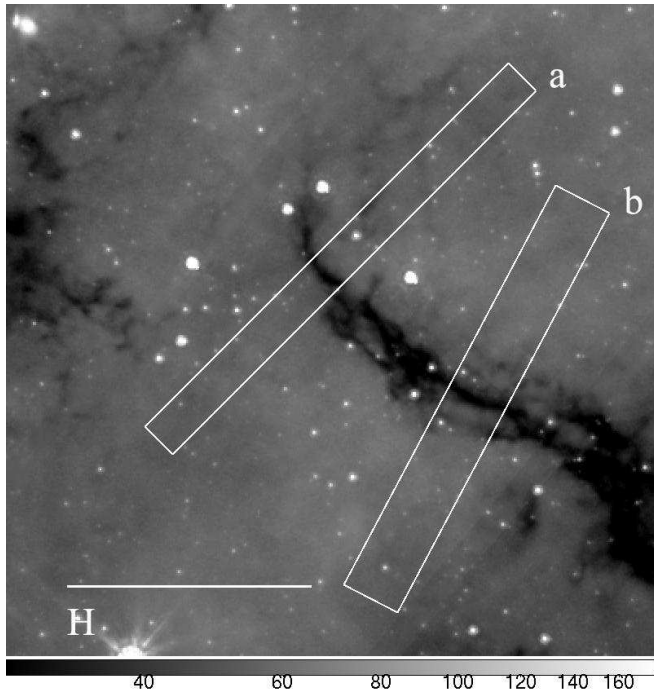


FIG. 5.— GLIMPSE  $8\mu\text{m}$  image of Cloud H with  $3'$  scale bar showing the strips considered in §3.2.3 (logarithmic intensity scale in units of  $\text{MJy sr}^{-1}$ ).

show the derived column densities. We see that the variations in the background estimates are relatively small, at approximately the 10% level, similar to the variations between the LMF and SMF methods seen in cloud C, and again corresponding to mass surface density uncertainties of  $\simeq 0.013 \text{ g cm}^{-2}$ .

#### 4. RESULTS

##### 4.1. Mass Surface Density Maps and Distributions

The mass surface density maps derived using the SMF method for the remaining 9 clouds are presented in Figures 7—9 with a uniform scale range in  $\Sigma$ . These IRDCs exhibit a variety of morphologies, ranging from very filamentary (clouds F and H) to those with more apparently spherical distributions (clouds C and E). The derived mass surface densities range up to  $\simeq 0.35 \text{ g cm}^{-2}$ , which is likely to be dependent on the angular resolution of the images. As is apparent from the  $8 \mu\text{m}$  images, some of the clouds have a few apparently embedded sources, which cause localized regions in the clouds to be IR-bright, and thus not amenable to our extinction mapping technique.

In figure 10 we show the mass-weighted probability distribution functions (PDFs) with  $\Sigma$  (evaluated with the SMF method) of the 10 IRDCs using the regions inside their Simon et al. (2006a) ellipses. Here we define  $M'$  as the mass fraction, normalized over the distribution of pixels with  $\Sigma > 0$ . In figure 11 we show the same PDF but now as a function of  $\Sigma/\bar{\Sigma}$ , where  $\bar{\Sigma}$  is the mean  $\Sigma$  (area-weighted over pixels which have  $\Sigma > 0$ ). The values of  $\bar{\Sigma}$  are listed in Table 1.

The distributions of  $\Sigma/\bar{\Sigma}$  show the most similarity for  $\Sigma/\bar{\Sigma} < 0.5$ . The high-side of the distributions do show a wide variety of profiles: there is a large range of mass

fractions at mass surface densities that are, for example, 3 times greater than the mean. Cloud J has the narrowest PDF, while cloud C has the broadest and one of the most skewed distributions. We caution that our derived IRDC PDFs are likely to be sensitive to the geometry of the ellipse that was chosen to represent the IRDC. For example this can affect the normalization of  $\bar{\Sigma}$  (although note we restrict its calculation over only the area of the cloud for which we measure  $\Sigma > 0$ ).

In the lower panel of Figure 11 we make a qualitative comparison of these results with the shapes of  $\Sigma/\bar{\Sigma}$  PDFs resulting from different astrophysical sources of turbulence as modeled in two sets of published numerical simulations. Offner, Klein, & McKee (2008) presented simulations of isothermal driven turbulence to maintain a mean 1D Mach number of about 5 in which self-gravity was then turned on at a particular time. One expects clouds with higher Mach number turbulence to have broader PDFs of  $\Sigma/\bar{\Sigma}$ , as stronger shocks lead to greater contrasts between regions of compression and rarefaction. Clouds that are more strongly self-gravitating also have broader PDFs. Self-gravity also tends to skew the PDFs towards the high-value side. Figure 11 shows two examples from these simulations: one is before self-gravity has been initiated, so is representative of the  $\Sigma/\bar{\Sigma}$  PDF from hydrodynamic Mach 4.7 (1D) driven turbulence with a Burgers  $P(k) \propto k^{-2}$  power spectrum; the other, which has a similar Mach number of 4.9, is after self-gravity has been allowed to develop structures for about 1 mean simulation free-fall time while the turbulence is still being driven and is somewhat broader as a result (14.2% of the gas mass has collapsed into sink particles by this time; the PDF is normalized to the total remaining gas mass).

Nakamura & Li (2007) presented simulations of magnetized protostellar outflow driven turbulence. The driving scale is relatively small compared to the simulation box, and the sources are centrally concentrated in the box. Their formation is sporadic as the global clump collapses: we show results after 1.5 global gravitational collapse times, when about 80 protostars have formed. Furthermore there is a large scale direction to the initial magnetic field, which has a mean dimensionless flux-to-mass ratio of 0.52 (in units of the critical value,  $2\pi G^{1/2}$  [Nakano & Nakamura 1978]), decreasing to 0.19 in the clump center. The mean value corresponds to about  $75 \mu\text{G}$  for the fiducial simulation parameters. This inhibits perpendicular motions, as can be seen from the narrowness of the  $\Sigma/\bar{\Sigma}$  PDF derived looking along the field direction compared to perpendicular to it (Figure 11; these distributions correspond to the models shown in Figure 7 of Nakamura & Li [2007]).

A comparison of the observed and simulated  $\Sigma/\bar{\Sigma}$  PDFs shows that the ensemble of the observed distributions can be qualitatively accounted for by the range of simulations shown, although the observed IRDCs generally have narrower distributions. However, we are not able to exclude the possibility that other numerical models involving different physics, e.g. a larger degree of magnetic support, and/or other parameters could not also explain the observed clouds. Since most of the IRDCs have relatively narrow PDFs compared to the Mach 5 turbulence models, this may indicate that these

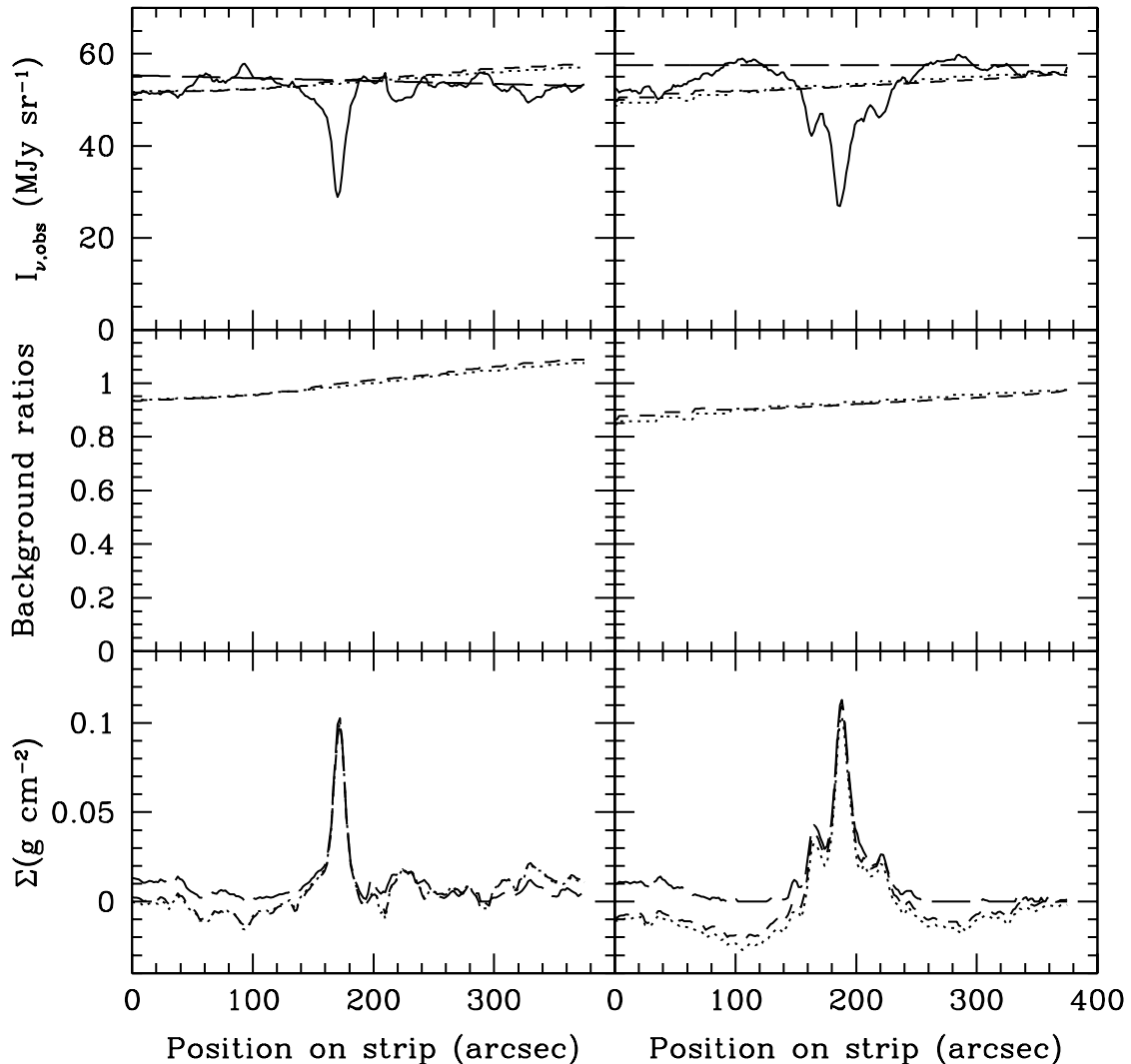


FIG. 6.— Results of LMF and SMF methods with thin strip analyses for strip a (left column) and strip b (right column). *Top* panels: Median  $I_{\nu, 1, \text{obs}}$  along the strip (solid lines), LMF estimate of  $I_{\nu, 0, \text{obs}}$  (dotted lines), SMF estimate of  $I_{\nu, 0, \text{obs}}$  (dashed lines), estimate from strip intensity profile (long dashed lines). Position coordinate increases from lower-left end of strips (see Fig. 5). *Middle* panels: Ratio of LMF (dotted) and SMF (dashed) estimates of  $I_{\nu, 0, \text{obs}}$  compared to estimate from the strip intensity profiles. *Bottom* panels: Estimates of  $\Sigma$  via LMF (dotted), SMF (dashed), and strip analysis (long dashed) methods.

clouds have smaller turbulent velocity dispersions and/or that dynamically important magnetic fields are present. The protostellar outflow driven turbulence models generally have broader  $\Sigma/\bar{\Sigma}$  PDFs than the observed IRDCs, and this may indicate these models are more applicable to later evolutionary stages of star cluster formation. However, they do illustrate the effects of dynamically important large-scale magnetic fields in creating narrower  $\Sigma/\bar{\Sigma}$  PDFs for viewing directions along the field lines.

Observations of the velocity structure of these IRDCs as traced by molecular line emission can help to further test the nature of turbulence present in the early stages of star cluster formation. The extinction mapping technique we have presented also opens up the possibility of studying the  $\Sigma/\bar{\Sigma}$  PDF as a function of IRDC  $\Sigma$ ,  $M$

and embedded stellar content. We defer a more quantitative study of these dependencies and a quantitative comparison of the  $\Sigma/\bar{\Sigma}$  PDFs to those formed in numerical simulations to a future study.

#### 4.2. Cloud and Core Masses

Given the (kinematic) distance to each cloud (Simon et al. 2006a), we convert our  $\Sigma$  estimates into mass estimates. For a typical distance of 3 kpc, each  $2.0''$  resolution element at  $8 \mu\text{m}$  (i.e. the mean FWHM of the point response function) corresponds to a linear scale of 0.029 pc, and if this has a typical  $\Sigma$  of  $0.1 \text{ g cm}^{-2}$ , this corresponds to a mass of  $0.41 M_{\odot}$ . We see that the mid-IR extinction mapping technique has the potential to probe relatively low mass scales.

In Table 1 we list the total cloud masses derived by



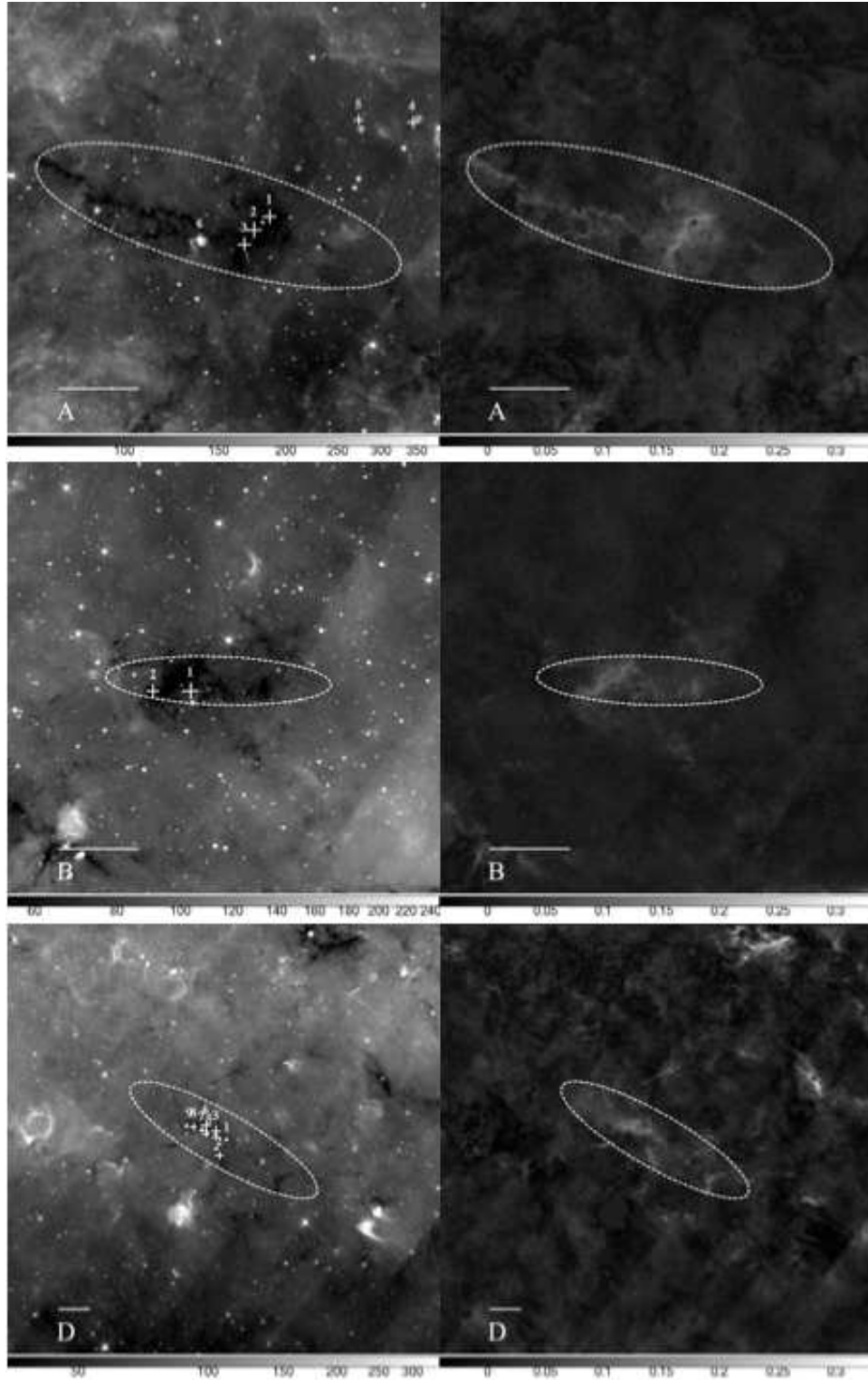


FIG. 7.— The *left* column shows Spitzer IRAC  $8\mu\text{m}$  images of IRDCs, with the dashed ellipse defined by Simon et al. (2006a) (based on MSX images), the crosses showing mm emission cores (Rathborne et al. 2006), with the numbers referring to their designation in Table 3, and the horizontal line showing a scale of  $3'$ . The *right* column shows extinction maps made by the small-scale median filtering method (SMF). From *top* to *bottom*, the clouds are: Cloud A (G018.82–00.28), Cloud B (G019.27+00.07), Cloud D (G028.53–00.25).

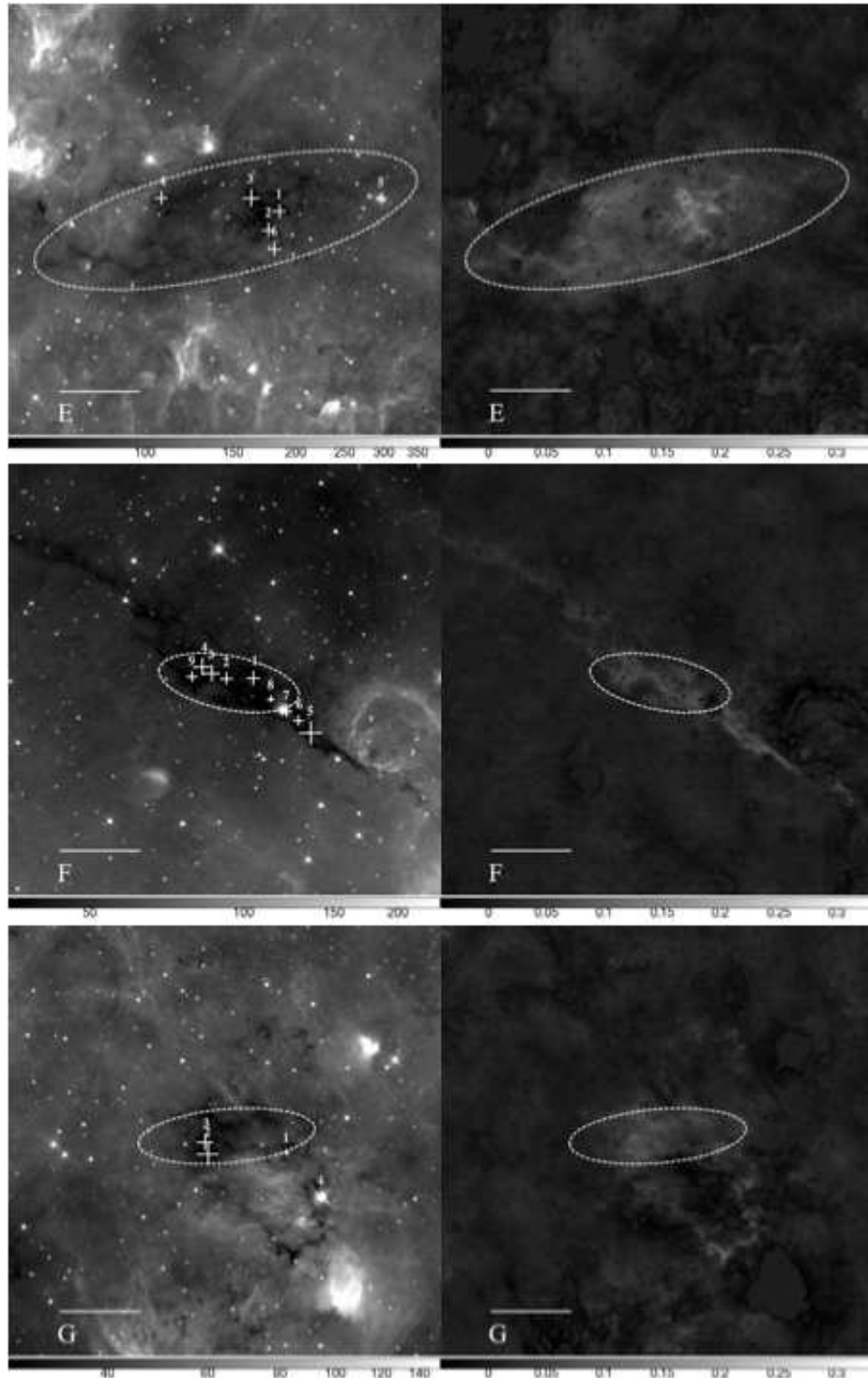


FIG. 8.— Same as Figure 7, but now, from *top to bottom*, the clouds are: Cloud E (G028.67+00.13), Cloud F (G034.43+00.24), Cloud G (G034.77–00.55).

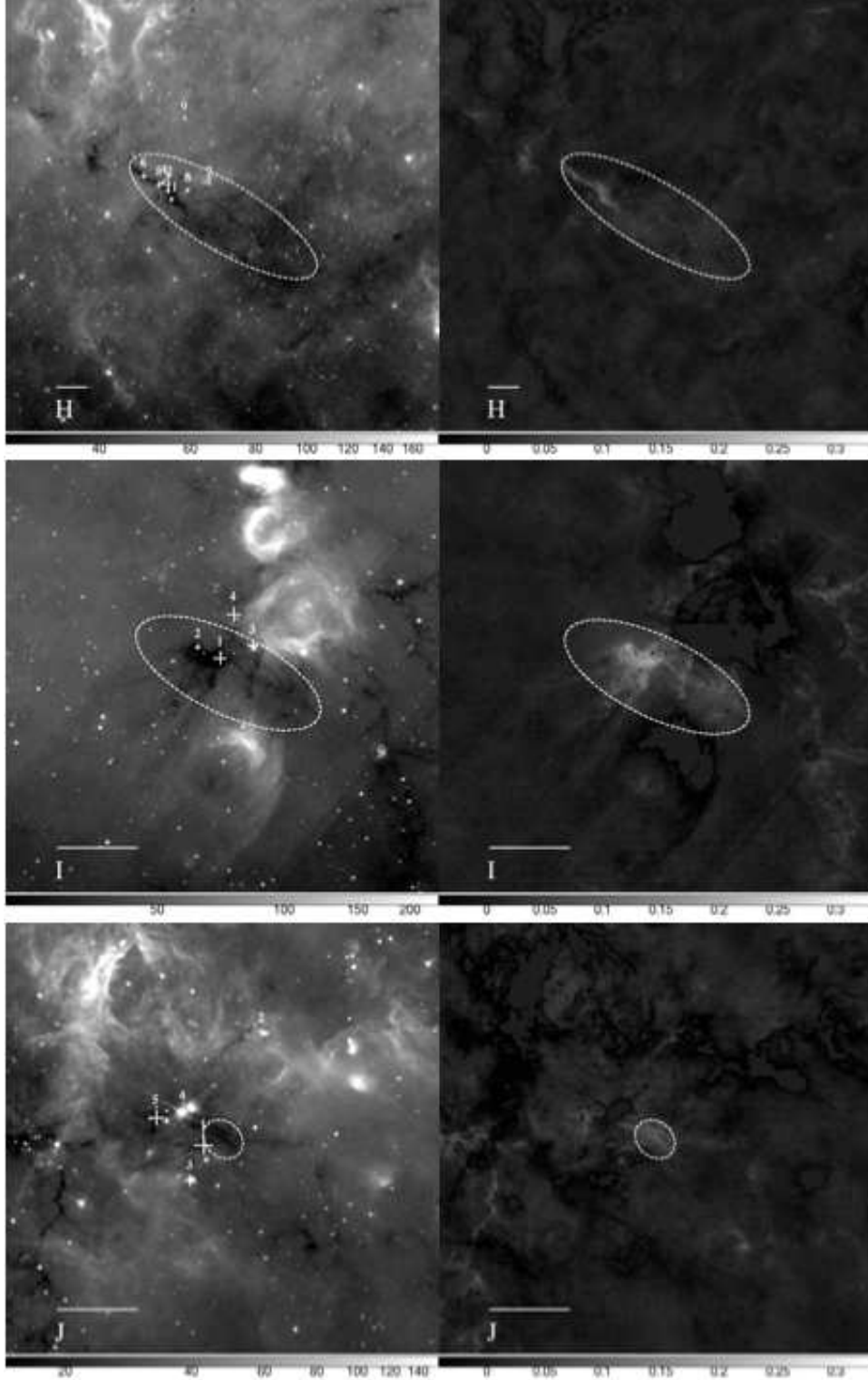


FIG. 9.— Same as Figure 7, but now, from *top to bottom*, the clouds are: Cloud H (G035.39–00.33), Cloud I (G038.95–00.47), Cloud J (G053.11+00.05).

the LMF and SMF extinction mapping methods. Note, these are the masses inside the elliptical regions defined by Simon et al. (2006a) from MSX images, and thus are not necessarily particularly close representations of the morphologies revealed by *Spitzer* IRAC. We find a mean

fractional difference of 35% between these two mass estimates. We regard the SMF mass estimate as being more accurate. Uncertainties in both methods will grow for larger clouds with lower mean mass surface densities (i.e. smaller contrasts against the background). Note

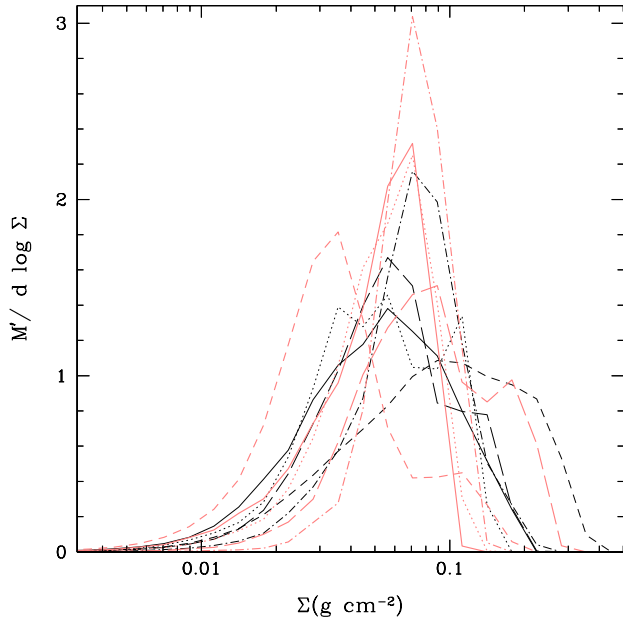


FIG. 10.— Mass-weighted probability distribution function ( $M'$  is the mass fraction) of  $\Sigma$  for clouds A (thin solid black line), B (thin dotted black), C (thin dashed black), D (thin long-dashed black), E (thin dot-dashed black), F (thick solid gray [pink in electronic version]), G (thick dotted gray), H (thick dashed gray), I (thick long-dashed gray), J (thick dot-dashed gray).

also this extinction mapping technique is not sensitive to a uniform screen of matter that covers both the region of the IRDC and the region where the background is estimated. A comparison of extinction-derived cloud masses and mass surface densities with the properties inferred by molecular line emission, such as  $^{13}\text{CO}$ , will be presented in a separate study (A. K. Hernandez & J. C. Tan, in prep.).

The extinction mass estimates are expected to become more accurate at high values of  $\Sigma$ . Each of the IRDCs in our sample contains dense cores studied by their mm dust continuum emission by Rathborne et al. (2006). We first identify those cores which are amenable to extinction mapping (i.e. do not contain bright  $8\ \mu\text{m}$  emission). Cores identified by Rathborne et al. (2006) as being mid-IR bright (labelled “(e)” in Table 3) were excluded. We also excluded cores overlapping with fainter IR sources, if the area affected by the sources was greater than about 10% of the core. Finally, we excluded cores with very low surface densities,  $\Sigma < 0.02\ \text{g cm}^{-2}$ , since the extinction mapping method becomes very unreliable at these levels due to uncertainties in the background estimation.

For our selected cores, we summed the mass inside a circular area centered on each core position with radius equal to half the angular FWHM diameter of Gaussian fits that Rathborne et al. (2006) fitted to their mm continuum images. Note the quoted angular FWHM diameters are typically about a factor of 1.09 times larger than the deconvolved FWHM diameters, so our areal integration actually extends out to about 0.545 true FWHM diameters from the core center. The total core masses quoted by Rathborne et al., which are evaluated by in-

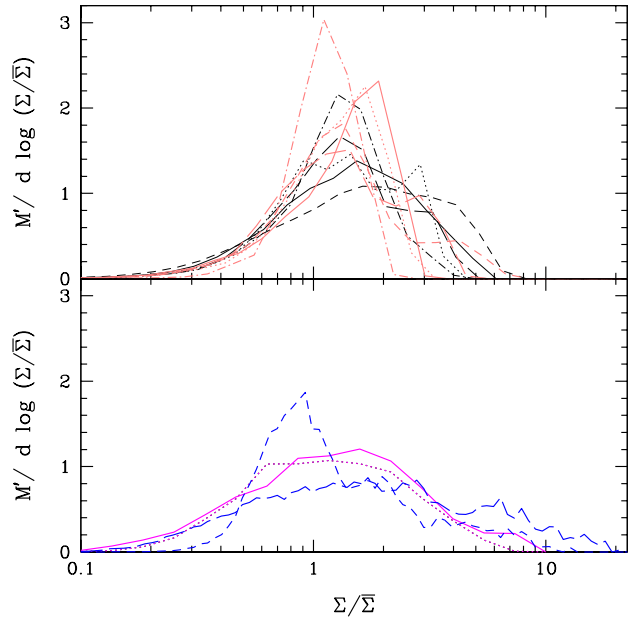


FIG. 11.— *Top*: Mass-weighted probability distribution function of  $\Sigma/\bar{\Sigma}$  for clouds A (thin solid black line), B (thin dotted black), C (thin dashed black), D (thin long-dashed black), E (thin dot-dashed black), F (thick solid gray [pink in electronic version]), G (thick dotted gray), H (thick dashed gray), I (thick long-dashed gray), J (thick dot-dashed gray). Note, cloud J has the most sharply-peaked, narrowest distribution, while cloud C has the broadest. *Bottom*: Comparison to simulations of astrophysical turbulence. Dotted line shows the result of Offner et al. (2008) for driven (Mach 4.7) turbulence with no self-gravity. Solid line shows the same simulation after self-gravity has been allowed to operate for 1 mean free fall time. The long-dashed line shows the result of Nakamura & Li (2007) for protostellar driven turbulence after 1.5 global gravitational collapse times as an average of two orthogonal viewing angles that are both perpendicular to the mean large-scale B-field in the simulation. The dashed line shows the view along the mean B-field.

tegrating over the whole 2D Gaussian distribution, will thus be a factor of 1.78 larger than that contained in this angular area, so we reduce their masses by a factor of 0.562. Their mass estimates involved assuming  $T = 15\ \text{K}$ , a dust opacity per mass of dust of  $\kappa_{1.2\text{mm}} = 1.0\ \text{cm}^2\ \text{g}^{-1}$  (Ossenkopf & Henning 1994), a gas-to-dust mass ratio of 100, and graybody emission with emissivity index  $\beta = 2$ . In the context of the Ossenkopf & Henning (1994) dust model with thin ice mantles, coagulated for  $10^5\ \text{yr}$  at  $n_{\text{H}} = 10^6\ \text{cm}^{-3}$ , which is the closest to our adopted  $8\ \mu\text{m}$  opacity, the interpolated 1.2 mm opacity is  $1.056\ \text{cm}^2\ \text{g}^{-1}$ , i.e. 5.6% higher than assumed by Rathborne et al. (2006), so we further reduce their masses by a factor 0.947. Our calculation of  $\Sigma$  from dust extinction assumed a gas-to-dust ratio of 156, which was that adopted for the Ossenkopf & Henning (1994) coagulation model. If this same ratio is applied to the mm emission masses, then the derived masses would be raised by 1.56 from the Rathborne et al. estimates. These three effects imply the Rathborne et al. quoted core masses should be reduced by a factor of 0.830 for a fair comparison with our extinction masses. Note, we use the same distance adopted by Rathborne et al. to the cores. In Table 3 and Figure 12 we compare the mm dust emission and mid-IR

dust extinction mass estimates.

We find generally very good agreement between these different methods. The dispersion in the ratios of the LMF and SMF estimates is about 15%. Comparing to the mm emission masses, the logarithmic average of  $M_{\text{mm}}/M_{\text{SMF}}$  is 1.08 with a dispersion of a factor of 1.8. This small systematic offset may be somewhat fortuitous given the systematic errors inherent to both methods. The possibility of correlations of  $M_{\text{mm}}/M_{\text{SMF}}$  with core properties is discussed below.

#### 4.3. Correlations of Core $M_{\text{mm}}/M_{\text{SMF}}$ with Density as Evidence for Grain Growth

We also use our SMF extinction mass to calculate a volume-averaged H number density in each core,  $\bar{n}_{\text{H,SMF}}$ , assuming spherical geometry. We find values in the range  $\bar{n}_{\text{H,SMF}} \simeq 10^4 - 10^5 \text{ cm}^{-3}$ . We examine the ratio of  $M_{\text{mm}}/M_{\text{SMF}}$  as a function of core density in Figure 13. The best fit power law relation is  $(M_{\text{mm}}/M_{\text{SMF}}) \propto \bar{n}_{\text{H,SMF}}^{-0.33}$ . Considering the Spearman rank-order correlation, the probability of a chance correlation is 0.0036. Since  $M_{\text{SMF}}$  and  $\bar{n}_{\text{H,SMF}}$  are correlated via the observable  $\Sigma_{\text{SMF}}$ , we also examine the correlation of  $(M_{\text{mm}}/M_{\text{SMF}})$  with  $M_{\text{SMF}}$ ,  $\Sigma_{\text{SMF}}$  (Figure 12), core radius,  $r$ , and core distance (Figure 13). We find probabilities of chance (anti)correlation of 0.28, 0.018, 0.99, and 0.43 respectively, i.e. there is no significant correlation of  $(M_{\text{mm}}/M_{\text{SMF}})$  with  $M_{\text{SMF}}$ ,  $r$ , and distance, and there is a marginally significant anticorrelation with  $\Sigma_{\text{SMF}}$ . The most significant trend is the anticorrelation of  $(M_{\text{mm}}/M_{\text{SMF}})$  with density.

One possible explanation for this observed trend is a systematic change in dust opacities at  $8\mu\text{m}$  and  $1.2 \text{ mm}$  caused by grain growth, since  $M_{\text{mm}}/M_{\text{SMF}} \propto \kappa_{8\mu\text{m}}/\kappa_{1.2\text{mm}}$ . For example, the thin ice mantle model of Ossenkopf & Henning (1994) predicts  $\kappa_{\text{IRAC}8\mu\text{m}}/\kappa_{1.2\text{mm}}$  decreases by a factor of 0.68 after coagulation for approximately  $10^6 \text{ yr}$  at a density of  $n_{\text{H}} = 10^5 \text{ cm}^{-3}$  (or  $10^7 \text{ yr}$  at a density of  $n_{\text{H}} = 10^4 \text{ cm}^{-3}$ ). The ratio decreases only slightly in the limit of further coagulation. Comparison of the uncoagulated bare grain and thin ice mantle models of Ossenkopf & Henning (1994) shows that  $\kappa_{8\mu\text{m}}/\kappa_{1.2\text{mm}}$  decreases by about a factor of 0.75 by the formation of ice mantles. Thus a total factor of about 0.5 decrease in  $M_{\text{mm}}/M_{\text{SMF}}$ , i.e. about that observed in our cores as the mean density changes from  $\sim 10^4 \text{ cm}^{-3}$  to  $\sim 10^5 \text{ cm}^{-3}$ , could be explained by a combination of ice mantle formation and grain growth. Note the typical density in the cores could be higher than the mean volume averaged value if they are clumpy.

Systematic temperature changes may also lead to changes in  $M_{\text{mm}}/M_{\text{SMF}}$ , via the estimate of  $M_{\text{mm}}$ . One does expect colder temperatures at higher densities, which would lead to  $M_{\text{mm}}$  being relatively underestimated at high densities under the constant temperature assumption of Rathborne et al. (2006). For example, adopting a temperature of 10 K rather than 15 K would raise  $M_{\text{mm}}$  by a factor of 1.9, which is enough to account for the observed trend of  $M_{\text{mm}}/M_{\text{SMF}}$  with density.

We conclude that this IRDC core population, as the mean density increases from  $\sim 10^4 \text{ cm}^{-3}$  to  $\sim 10^5 \text{ cm}^{-3}$ , shows tentative evidence for either opacity changes that are consistent with models of ice mantle formation and

grain coagulation, or a temperature decrease of  $\sim 5 \text{ K}$ . Systematic follow up of these cores with  $\text{NH}_3$  observations to measure temperature, as has been done in some IRDCs (e.g. Sridharan et al. 2005; Pillai et al. 2006; Wang et al. 2008), can help to distinguish these possibilities.

Evidence for grain growth has previously been reported in the low-mass core B68 by Bergin et al. (2006), based on low gas-to-dust temperature coupling rates. Bianchi et al. (2003) considered ratios of  $850 \mu\text{m}$  and  $1.2 \text{ mm}$  opacities to visual opacities in B68, finding no conclusive evidence for grain growth. Keto & Caselli (2008) require increased dust opacities due to large, fluffy grains to explain the  $\leq 7 \text{ K}$  temperatures observed in the centers of some low-mass starless cores. Flower, Pineau des Forêts, & Walmsley (2005, 2006) considered the chemical implications of grain growth, finding it causes an increase in the electron fraction and the ratio of  $\text{H}^+/\text{H}_3^+$ , and can have moderate effects on the observed differential freeze-out of nitrogen and carbon bearing species. Vastel et al. (2006) required grains larger than  $0.3\mu\text{m}$  to reproduce the ortho- $\text{H}_2\text{D}^+$  observations in the prestellar core L1544. A systematic molecular line study of our studied IRDC cores to test for the above chemical effects and any correlation with  $M_{\text{mm}}/M_{\text{SMF}}$  would be useful.

## 5. CONCLUSIONS

We have presented a new method of diffuse mid-IR ( $8\mu\text{m}$ ) extinction mapping of infrared dark clouds to probe the initial conditions for massive star and star cluster formation. The technique can naturally probe to higher mass surface densities than NIR extinction mapping using background stars and provides an estimate of the mass surface density at scales that are only limited by the resolution of the mid-IR image (e.g. a couple of arcseconds for *Spitzer* IRAC). However, the method involves a spatial interpolation and smoothing of the diffuse background, which inevitably introduces additional uncertainties. In particular it is a relative mass surface density of the cloud compared to the region used to ascertain the background that is derived. Also, small scale background fluctuations are not captured and local regions containing mid-IR bright sources cannot be treated. One of the largest uncertainties for more distant clouds is the correction for foreground mid-IR emission from hot dust, and so we have generally restricted the analysis to relatively nearby clouds.

We have examined three different methods of estimating the diffuse background behind IRDCs. The Large-scale Median Filter (LMF) method is the simplest by not requiring information about the cloud size or location, but then must smooth over relatively large scales. The Small-scale Median Filter (SMF) achieves higher spatial resolution of the background given defined cloud boundaries, and we generally regard this method as being more accurate where such information is available. Finally, for very thin, filamentary clouds, more detailed background fitting can be attempted by considering perpendicular strips across the filament. Comparing these methods on a sample of 10 IRDCs we find systematic differences due to background fitting at about the 10% level. This means that the mid-IR extinction mapping technique becomes unreliable for  $\Sigma \lesssim 0.013 \text{ g cm}^{-2}$  (given our adopted fiducial  $8 \mu\text{m}$  [*Spitzer* IRAC Band 4 and diffuse Galactic

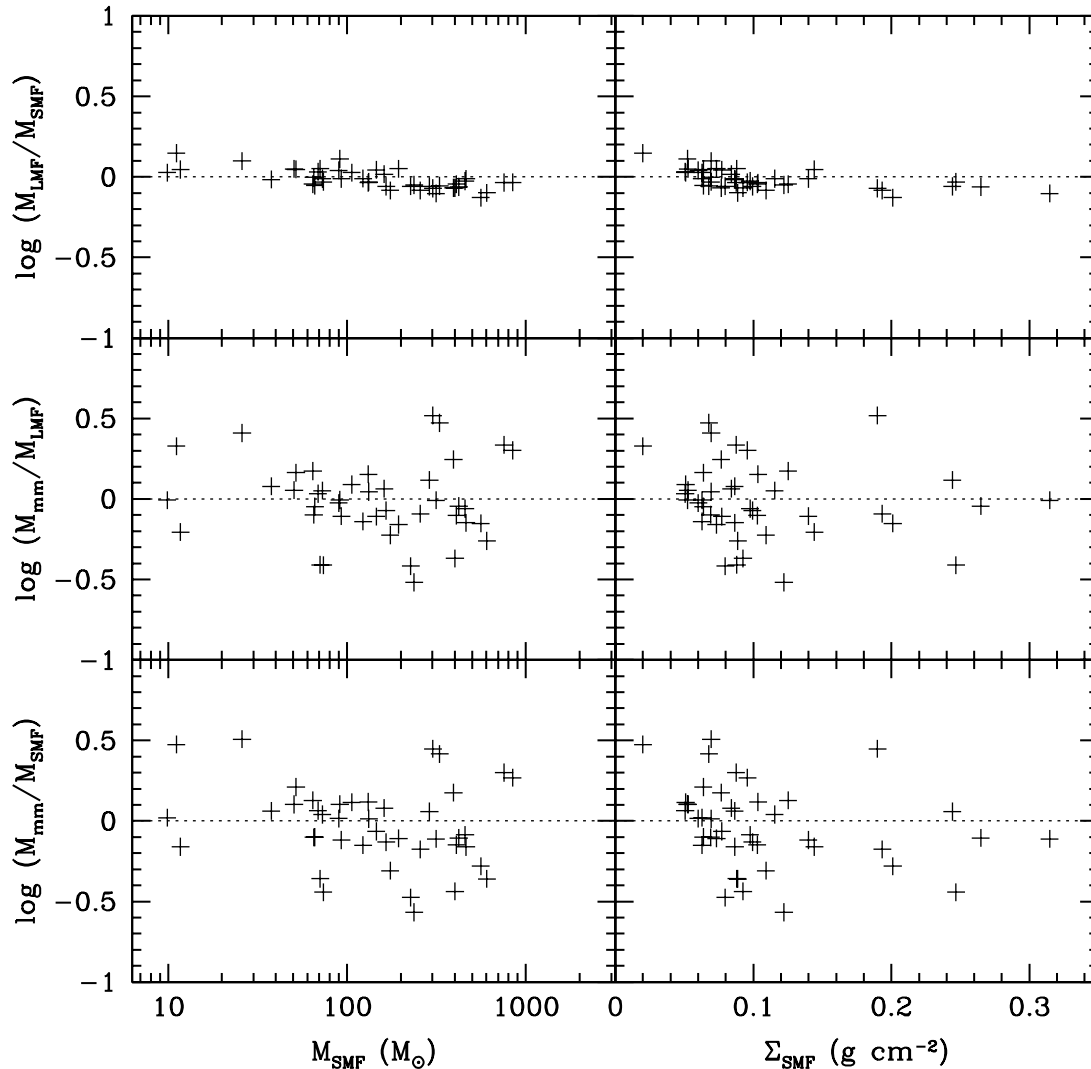


FIG. 12.— Comparison of core mass estimates. *Top Left*: Ratio of cores masses determined via extinction mapping with Large and Small Median Filter methods ( $M_{\text{LMF}}/M_{\text{SMF}}$ ) versus core mass. *Top right*: Same data plotted as a function of core  $\Sigma$  (estimated via the SMF method). *Middle panels*: Ratio of mm emission mass (Rathborne et al. 2006) to  $M_{\text{LMF}}$ . *Bottom panels*: Ratio of mm emission mass to  $M_{\text{SMF}}$ .

background spectrum weighted] opacity of  $7.5 \text{ cm}^2 \text{ g}^{-1}$ ).

We have then used this method to measure the mass surface densities of the 10 IRDCs. The probability distribution functions of  $\Sigma$  for these clouds show a range of shapes, that is qualitatively consistent with that expected in numerical simulations of turbulence, though the relatively narrow distributions of the observed clouds indicate that the Mach numbers are probably  $\lesssim 5$  and/or that magnetic fields are dynamically important. A more quantitative comparison of the observed clouds with numerical models, and a search for evolutionary trends associated with the development of self-gravitating structures is planned for a future study.

Given IRDC kinematic distances, we then estimate masses of the clouds and, more accurately, of their dense cores. Comparing to mass estimates from mm dust continuum emission (Rathborne et al. 2006) we find very

good agreement: a  $\lesssim 10\%$  systematic offset for the population of 43 studied cores, and a dispersion of less than a factor of two in the distribution.

Finally, we examine the ratio of masses estimated by mm dust emission to those found from mid-IR dust extinction as a function of core density, tentatively finding a trend which can be explained as being due to opacity changes due to ice mantle formation and grain growth or by a temperature decrease of about 5 K in the densest cores. Future studies of the mid-IR extinction law in these cores and molecular line studies of their chemistry can help to test the reality of this result and distinguish between these explanations.

We thank Stella Offner, Richard Klein, Christopher McKee, Fumitaka Nakamura and Zhi-Yun Li for provid-

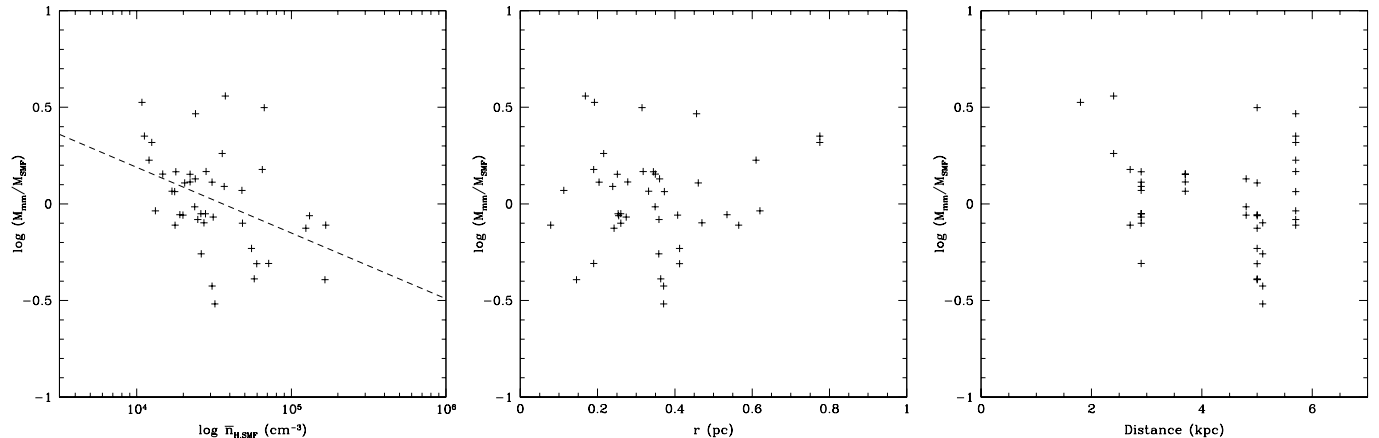


FIG. 13.— *Left panel:* Ratio of core masses estimated from mm dust emission and  $8\ \mu\text{m}$  extinction with the SMF method ( $M_{\text{mm}}/M_{\text{SMF}}$ ) versus mean volume density,  $\bar{n}_{\text{H,SMF}}$ . The dashed line shows the best fit power law relation,  $(M_{\text{mm}}/M_{\text{SMF}}) \propto \bar{n}_{\text{H,SMF}}^{-0.33}$ . The significance of this anticorrelation is discussed in the text. *Middle panel:* Ratio of  $(M_{\text{mm}}/M_{\text{SMF}})$  versus core radius. No significant trend is observed (see text). *Right panel:* Ratio of  $(M_{\text{mm}}/M_{\text{SMF}})$  versus core distance. No significant trend is observed (see text).

ing us with mass surface density data from their numerical simulations. We thank Cara Battersby, Robert Benjamin, Paola Caselli, Bruce Draine, Eric Ford, James

Jackson, Mark Krumholz, & Jill Rathborne for helpful discussions. JCT acknowledges support from NSF CAREER grant AST-0645412.

#### REFERENCES

- Benjamin, R. A., Churchwell, E., Babler, B. L., Bania, T. M., Clemens, D. P. et al. 2003, *PASP*, 115, 953
- Bergin, E. A., Maret, S., van der Tak, F. F. S., Alves, J., Carmody, S. M., & Lada, C. J. 2006, *ApJ*, 645, 369
- Bianchi, S., Goncalves, J., Albrecht, M., Caselli, P., Chini, R., Galli, D., & Walmsley, M. 2003, *A&A*, 399, L43
- Bonnell, I. A., Bate, M. R., & Zinnecker, H. 1998, *MNRAS*, 298, 93
- Bonnell, I. A., Bate, M. R., Clarke, C. J., & Pringle, J. E. 2001, *MNRAS*, 323, 785
- Bonnell, I. A., Vine, S. G., & Bate, M. R. 2004, *MNRAS*, 349, 735
- Carey, S. J., Clark, F. O., Egan, M. P., Price, S. D., Shipman, R. F., & Kuchar, T. A. 1998, *ApJ*, 508, 721
- Dalgarno, A., & Lepp, S. 1984, *ApJ*, 287, L47
- de Wit, W. J., Testi, L., Palla, F., & Zinnecker, H. 2005, *A&A*, 437, 247
- Draine, B. T. 2003, *ARA&A*, 41, 241
- Egan, M. P., Shipman, R. F., Price, S. D., Carey, S. J., Clark, F. O., Cohen, M. 1998, *ApJ*, 494, L199
- Elmegreen, B. G. 2000, *ApJ*, 530, 277
- Elmegreen, B. G. 2007, *ApJ*, 668, 1064
- Flower, D. R., Pineau des Fôrets, G., Walmsley, C. M. 2005, *A&A*, 436, 933
- Flower, D. R., Pineau des Fôrets, G., Walmsley, C. M. 2006, *A&A*, 456, 215
- Hartmann, L. & Burkert, A. 2007, *ApJ*, 654, 988
- Hester, J. J., Desch, S. J., Healy, K. R., & Leshin, L. A. 2004, *Science*, 304, 1116
- Indebetouw, R., et al. 2005, *ApJ*, 619, 931
- Jackson, J. M. et al. 2006, *ApJS*, 163, 145
- Kennicutt, R. C., 1998, *ApJ*, 498, 541
- Keto, E. & Caselli, P. 2008, *ApJ*, 683, 238
- Lada, C. J., & Lada, E. A. 2003, *ARA&A*, 41, 57
- Li, A., & Draine, B. T. 2001, *ApJ*, 554, 778
- Lutz, D. et al. 1996, *A&A*, 315, L269
- McKee, C. F., & Tan, J. C. 2003, *ApJ*, 585, 850
- McKee, C. F., & Williams, J. P. 1997, *ApJ*, 476, 144
- Nakamura, F. & Li, Z.-Y. 2007, *ApJ*, 662, 395
- Nakano, T., & Nakamura, T. 1978, *PASJ*, 30, 681
- Offner, S. S. R., Klein, R. I., McKee, C. F. 2008, *ApJ*, 686, 1174
- Ossenkopf, V., & Henning, T. 1994, *A&A*, 291, 943
- P  rault, M. et al. 1996, *A&A*, 315, L165
- Pillai, T., Wyrowski, F., Carey, S. J., & Menten 2006, *A&A*, 450, 569
- Pillai, T., Wyrowski, F., Hatchell, J., Gibb, A. G., & Thompson, M. A. 2007, *A&A*, 467, 207
- Ragan, S. E., Bergin, E. A., Plume, R., Gibson, D. L., Wilner, D. J., O’Brien, S., Hails, E. 2006, *ApJS*, 166, 567
- Rathborne, J. M., Jackson, J. M., & Simon, R. 2006, *ApJ*, 641, 389
- Rom  n-Z  niga, Lada, C. J., Muench, A., & Alves, J. F. 2007, *ApJ*, 664, 357
- Sakai, T., Sakai, N., Kamegai, K., Hirota, T., Yamaguchi, N., Shiba, S., Yamamoto, S. 2008, *ApJ*, 678, 1049
- Shu, F. H., Adams, F. C., & Lizano, S. 1987, *ARA&A*, 25, 23
- Simon, R., Jackson, J. M., Rathborne, J. M., Chambers, E. T. 2006a, *ApJ*, 639, 227
- Simon, R., Rathborne, J. M., Shah, R. Y., Jackson, J. M., & Chambers, E. T. 2006b, *ApJ*, 653, 1325
- Sridharan, T. K., Beuther, H., Saito, M., Wyrowski, F., & Schilke P. 2005, *ApJ*, 634, L57
- Tan, J. C., Krumholz, M. R., McKee, C. F. 2006, *ApJ*, 641, L121
- Vastel, C., Caselli, P., Ceccarelli, C., Phillips, T., Wiedner, M. C., Peng, R., Houde, M., & Dominik, C. 2006, *ApJ*, 645, 1198
- Wang, Y., Zhang, Q., Pillai, T., Wyrowski, F., Wu, Y. 2008, *ApJ*, 672, L33
- Weingartner, J. C., & Draine, B. T. 2001, *ApJ*, 548, 296

TABLE 3  
IRDC CORES

Core Name <sup>a</sup>	Galactic Coordinates		Diameter <sup>b</sup>	$M_{\text{mm}}^c$	$\bar{\Sigma}_{\text{LMF}}$	$\bar{\Sigma}_{\text{SMF}}$	$M_{\text{LMF}}$	$M_{\text{SMF}}$	$\bar{n}_{\text{H,SMF}}$
	$l$	$b$	(pc)	( $M_{\odot}$ )	( $\text{g cm}^{-2}$ )	( $\text{g cm}^{-2}$ )	( $M_{\odot}$ )	( $M_{\odot}$ )	( $10^5 \text{cm}^{-3}$ )
A1 (MM4)	18.790	-0.286	0.721	219	0.0829	0.0813	163	157	0.232
A2 (MM6)	18.799	-0.294	0.814	171	0.0805	0.0710	211	188	0.193
A3 (MM5)	18.806	-0.303	0.698	141	0.0805	0.0749	156	142	0.230
A4 (MM3)(e)	18.701	-0.227	0.582	194	-	-	-	-	-
A5 (MM1)(e)	18.735	-0.226	0.535	736	-	-	-	-	-
A6 (MM2)(e)	18.833	-0.299	0.465	201	-	-	-	-	-
B1 (MM2)	19.288	0.0824	0.431	94.5	0.0656	0.0631	57.3	51.3	0.354
B2 (MM1)	19.311	0.0675	0.337	93.7	0.0774	0.0687	32.2	25.7	0.370
C1 (MM9)	28.324	0.0677	0.824	330	0.165	0.194	401	539	0.532
C2 (MM4)	28.345	0.0597	0.509	274	0.234	0.304	239	303	1.26
C3 (MM11)	28.352	0.1008	0.921	371	0.199	0.235	243	279	0.197
C4 (MM6)	28.355	0.0726	0.485	192	0.162	0.186	204	248	1.20
C5 (MM14)	28.356	0.0566	0.291	30.0	0.188	0.238	66.1	71.1	1.59
C6 (MM10)	28.362	0.0532	0.824	296	0.0757	0.0857	465	584	0.576
C7 (MM16)	28.367	0.1203	1.07	371	0.203	0.256	352	406	0.183
C8 (MM17)	28.388	0.0381	0.727	164	0.0789	0.0892	329	387	0.556
C9 (MM1)(e)	28.399	0.0812	0.630	952	0.155	0.183	248	291	0.643
C10 (MM8)(e)	28.244	0.0127	0.751	343	-	-	-	-	-
C11 (MM7)(e)	28.292	0.0065	0.582	253	-	-	-	-	-
C12 (MM3)(e)	28.322	-0.0101	0.558	400	-	-	-	-	-
C13 (MM5)(e)	28.325	0.1613	0.412	147	-	-	-	-	-
C14 (MM12)(e)	28.328	-0.0388	1.02	395	-	-	-	-	-
C15 (MM2)(e)	28.337	0.1170	0.533	449	-	-	-	-	-
C16 (MM15)(e)	28.339	0.1424	0.630	111	-	-	-	-	-
C17 (MM18)(e)	28.417	-0.00726	0.824	135	-	-	-	-	-
C18 (MM13)(e)	28.419	0.1391	1.02	385	-	-	-	-	-
D1 (MM5)	28.526	-0.2503	0.636	194	0.0873	0.0995	117	126	0.271
D2 (MM7)	28.538	-0.2757	1.24	421	0.0799	0.0942	416	441	0.127
D3 (MM3)	28.543	-0.2369	1.55	1690	0.0722	0.0844	672	729	0.108
D4 (MM8)	28.543	-0.2651	0.746	154	0.0565	0.0669	119	127	0.169
D5 (MM2)	28.559	-0.2274	1.55	1760	0.0817	0.0924	753	813	0.121
D6 (MM4)	28.559	-0.2412	1.22	663	0.0707	0.0739	324	380	0.116
D7 (MM1)	28.565	-0.2350	0.912	1000	0.0603	0.0655	280	318	0.232
D8 (MM10)	28.579	-0.2303	1.13	360	0.0708	0.0836	435	447	0.171
D9 (MM9)	28.589	-0.2285	0.718	138	0.0829	0.0959	140	160	0.239
D10 (MM6)	28.557	-0.2382	0.497	98.6	-	-	-	-	-
E1 (MM7)	28.644	0.1375	0.742	72.2	0.109	0.119	206	230	0.311
E2 (MM5)	28.650	0.1260	0.742	85.4	0.0632	0.0774	193	221	0.298
E3 (MM2)	28.661	0.1456	0.940	327	0.0872	0.100	359	398	0.264
E4 (MM4)	28.717	0.1456	0.717	96.2	0.0953	0.106	140	169	0.254
E5 (MM3)	28.580	0.1456	0.544	101	-	-	-	-	-
E6 (MM6)	28.647	0.1143	0.766	93.7	-	-	-	-	-
E7 (MM1)	28.688	0.1782	0.495	119	-	-	-	-	-
F1 (MM8)	34.422	0.24792	0.556	89.6	0.0556	0.0497	72.8	67.8	0.217
F2 (MM7)	34.438	0.24759	0.502	72.2	0.0573	0.0517	55.8	49.8	0.217
F3 (MM6)	34.448	0.25091	0.664	104	0.0625	0.0591	97.0	88.4	0.166
F4 (MM9)	34.454	0.25495	0.699	130	0.0583	0.0513	116	89.7	0.145
F5 (MM5)	34.386	0.21378	0.915	550	-	-	-	-	-
F6 (MM4)	34.394	0.22156	0.431	211	-	-	-	-	-
F7 (MM2)	34.401	0.22709	0.466	1060	-	-	-	-	-
F8 (MM1)	34.411	0.23489	0.287	985	-	-	-	-	-
F9 (MM3)	34.459	0.24867	0.431	250	-	-	-	-	-
G1 (MM3)	34.734	-0.5670	0.225	11.6	0.0606	0.0622	10.4	9.77	0.474
G2 (MM2)	34.783	-0.5683	0.689	156	0.0515	0.0504	112	105	0.177
G3 (MM4)	34.784	-0.5608	0.506	58.0	0.0667	0.0682	64.1	64.6	0.275
G4 (MM1)	34.712	-0.5946	0.323	138	-	-	-	-	-
H1 (MM9)	35.478	-0.3096	0.380	34.8	0.0842	0.0869	78.7	69.9	0.705
H2 (MM4)	35.483	-0.2858	0.478	89.6	0.113	0.114	69.9	71.9	0.364
H3 (MM5)	35.483	-0.2954	0.520	97.9	0.0602	0.0621	119	122	0.477
H4 (MM8)	35.491	-0.2830	0.408	48.9	0.0830	0.0854	36.0	37.4	0.304
H5 (MM6)	35.497	-0.2863	0.520	58.8	0.0602	0.0629	57.8	65.3	0.257
H6 (MM7)	35.522	-0.2724	0.548	79.6	0.133	0.138	89.8	92.0	0.308
H7 (MM2)(e)	35.417	-0.2847	0.239	37.3	-	-	-	-	-
H8 (MM3)(e)	35.452	-0.2951	0.337	65.5	-	-	-	-	-
H9 (MM1)(e)	35.456	-0.1801	0.295	63.0	-	-	-	-	-
I1 (MM1)	38.957	-0.4659	0.380	97.0	0.111	0.124	57.3	63.6	0.640
I2 (MM3)	38.971	-0.4588	0.157	9.12	0.135	0.142	12.8	11.6	1.65
I3 (MM2)(e)	38.937	-0.4578	0.327	60.5	-	-	-	-	-
I4 (MM4)(e)	38.949	-0.4385	0.432	39.8	-	-	-	-	-



TABLE 3 — *Continued*

Core Name <sup>a</sup>	Galactic Coordinates		Diameter <sup>b</sup>	$M_{\text{mm}}^c$	$\bar{\Sigma}_{\text{LMF}}$	$\bar{\Sigma}_{\text{SMF}}$	$M_{\text{LMF}}$	$M_{\text{SMF}}$	$\bar{n}_{\text{H,SMF}}$
	$l$	$b$	(pc)	( $M_{\odot}$ )	( $\text{g cm}^{-2}$ )	( $\text{g cm}^{-2}$ )	( $M_{\odot}$ )	( $M_{\odot}$ )	( $10^5 \text{cm}^{-3}$ )
J1 (MM4)	53.128	0.0503	0.384	37.3	0.0324	0.0219	17.1	12.2	0.118
J2 (MM3)(e)	53.092	0.1201	0.166	9.94	-	-	-	-	-
J3 (MM5)(e)	53.136	0.0283	0.209	10.8	-	-	-	-	-
J4 (MM1)(e)	53.141	0.0717	0.183	103	-	-	-	-	-
J5 (MM2)(e)	53.157	0.0672	0.288	36.5	-	-	-	-	-

<sup>a</sup> Name in parentheses from Rathborne et al. (2006). “(e)” indicates their designation of the core as containing  $8 \mu\text{m}$  emission. We have identified additional cores that contain  $8 \mu\text{m}$  sources, for which we also do not calculate extinction mass surface densities and masses.

<sup>b</sup> Derived from the angular size of the FWHM of the Gaussian profile fitted to the core by Rathborne et al. (2006).

<sup>c</sup> Millimeter emission mass, from Rathborne et al. (2006).